

Anisotropic magnetoresistance and electronic fermiology in Dirac Node-Line material ZrSiSe

Haiyang Pan, Jihai Yu, Jue Wang, Dongzhi Fu, Shuai Zhang, Bin Wu, Xiangang Wan
& Fengqi Song*

National Laboratory of Solid State Microstructures, Collaborative Innovation Center
of Advanced Microstructures, College of Physics, Nanjing University, Nanjing
210093, P. R. China

*corresponding author: songfengqi@nju.edu.cn

ABSTRACT

The family of materials defined as $ZrSiX$ ($X = S, Se, Te$) has been established as Dirac node-line semimetals, and their Dirac Fermion behavior has been observed in previous experiments. In this study, we systematically investigate the angular-dependent magnetoresistance property and the corresponding Shubnikov–de Haas (SdH) oscillations in topological node-line semimetal ZrSiSe bulk crystals. The observed nonlinear Hall signal indicates the coexistence of multiple carrier types in the electrical transport. The angular-dependent magnetoresistance of a fixed magnetic field value shows strong anisotropy, which is associated with the quasi-2D electronic structure. SdH oscillation frequencies corresponding to 210 T and 30 T are identified, for which angle-dependent plots yield the corresponding electronic fermiology. A Fermi pocket with SdH frequency of 210 T indicates evident quasi-2D properties, which is attributed to the tubular-shaped Fermi surface near the X point in the Brillouin zone as per first-principles calculations.

Intensive studies focused on seeking optimized Dirac materials have led to the discovery of Dirac node-line materials (DNLMs), which originate from the strong degeneracy of band crossing points between the valence band and the conduction band in the Brillouin zone (BZ)¹⁻⁶. The band crossing points in DNLMs form extended lines or closed loops in the BZ, which therefore contribute to a carrier density of $\sim 10^{21} \text{ cm}^{-3}$ ^{7,8}, which is significantly larger than those of graphene and other Dirac semimetals⁹⁻¹⁸. Thus far, PbTaSe_2 ¹⁹, PtSn_4 ²⁰ and the *WHM* ($W = \text{Zr/Hf/La}$, $H = \text{Si/Ge/Sn/Sb}$, $M = \text{O/S/Se/Te}$)²¹ (when spin-orbit coupling (SOC) is ignored) compounds were speculated to be DNLMs, and this has been confirmed by angle-resolved photoemission spectroscopy (ARPES) measurements²²⁻²⁸. Particular attention has been paid to materials in the *WHM* family because they exhibit the space group of iron-based superconductors and their monolayers are suggested to be 2D topological insulators²¹. ARPES measurements have been used to observe a diamond-shaped Fermi surface hosting line nodes at the BZ center point and the symmetry-protected band crossing at the X point, thereby indicating the formation of the node-line semimetal (NLSM) phase as well as the appearance of nearly flat surface states around the X point^{22,23,25,28,29}. More detailed ARPES studies and theoretical band calculations on ZrSiX ($X = \text{S, Se, Te}$) reveal a transition from the node-line to the nodeless gapped phase when tuning the chalcogenide from S to Te²⁵. The gap opening (60 meV) results from increment of the SOC strength in ZrSiTe , and the gap can be ignored in ZrSiS and ZrSiSe . High mobility and nearly electron-hole-compensated carriers result in a high magnetoresistance (MR) ratio³⁰.

In this paper, we report on the angular-dependent electrical transport in ZrSiSe bulk crystals. At low temperatures, clear Shubnikov-de Haas (SdH) oscillations are observed, and the nonlinear-Hall-signal-dependent magnetic field reveals multiband features. The MRs corresponding to the *bc*-plane and *ac*-plane exhibit anisotropic behavior. Further, the SdH oscillations “construct” a quasi-2D Fermi pocket with an SdH frequency of 210 T, whose Fermi-surface cross-sectional area is consistent with the small pocket at X. The calculated band structure and Fermi surface further

confirm multiband contribution to the electrical transport and the tubular-shaped Fermi-pocket origin of the 210-T frequency oscillation.

Results and Discussions

Single crystals of ZrSiSe were synthesized by means of a chemical vapor transport method (see Methods). The synthesized ZrSiSe bulk crystals appeared as rectangular plate-like crystals with a metallic luster. Fig. 1(a) shows the X-ray diffraction image of the exposed plate-like surface of a ZrSiSe crystal. The presence of sharp (00L) peaks can be attributed to the (001) plane (*c*-plane) of the plate-like surface and the high crystallinity of ZrSiSe crystals. As shown in Fig. 1(b), the temperature-dependent resistivity of sample 1 at zero magnetic field exhibits metallic behavior and almost reaches saturation below 50 K. When the magnetic field is applied along the [001] direction (*c*-axis), the unsaturated MR ρ_{xx} with evident SdH oscillations can be observed at low temperature, and the MR ratio $\rho_{xx}(B)/\rho_{xx}(0)$ begins to decrease with increasing in temperature. The field-dependent Hall resistivity measured at various temperatures is depicted in Fig. 1(d), and SdH oscillations can be clearly observed at low temperatures (below 30 K), thereby implying the high carrier mobility in the measured ZrSiSe crystal. From 2 K to 100 K, the Hall resistivity ρ_{xy} exhibits a nearly nonlinear behavior and assumes nearly linear positive values at low field values. However, ρ_{xy} at high field values changes from positive to negative as the temperature increases. This indicates that multiple types of carriers play a role in the electrical transport in ZrSiSe. The theoretical band calculations and ARPES measurement reveal electron and hole Fermi pocket surfaces in ZrSiX ($X = \text{S}, \text{Se}, \text{Te}$)^{21,25,31}, which can explain the measured nonlinear Hall behavior in our electrical transport experiment.

To further investigate the MR electrical properties, we performed angular-dependent SdH-oscillation measurements along two main crystal planes (*bc*-plane and *ac*-plane) to study the entire Fermi surface in sam0ple 2. Here, we note that current I is always applied along the *a*-axis during the MR measurements. We

first measured the angular-dependent MR along the bc -plane as the magnetic field is always perpendicular to the current direction to maintain a constant Lorentz force. The inset of Fig. 2(a) shows the MR measurement scheme for the bc -plane. The magnetic field direction is indicated by ϕ , that is, the angle between the magnetic field and the c -axis on the bc -plane. Parameter $MR = [\rho(B) - \rho(0)]/\rho(0)$ is commonly used to illustrate the change in the resistivity amplitude due to the applied magnetic field B . The angular-dependent MR measurements with ϕ varying from 0° to 90° were carried out along the bc -plane at 2.3 K. In order to clearly observe the difference in MR oscillations, we only depict certain MR curves corresponding to different magnetic field directions in Fig. 2(a). Fig. 2(b) displays the polar plot of the angular-dependent MR for different magnetic field values. The MR curve exhibits the typical butterfly shape, as previously reported for $ZrSiS$ ^{7,30,32,33}, $ZrSiSe$ ⁷, and $HfSiS$ ³⁴ materials. The anisotropic feature of MR reveals the presence of a strong anisotropic electronic structure in $ZrSiSe$ crystals. As reported for $ZrSiS$, the butterfly-shaped MR can be regarded as twofold and fourfold symmetries³³, and this is very different from the anisotropic MR observed in WTe_2 ^{35,36}, $LaBi$ ³⁷, and Bi ^{38,39}. For a perfect 2D electronic structure, the angular-dependent MR exhibits typical twofold-symmetry anisotropy. In contrast, the MR is almost unchanged for a 3D isotropic electronic structure system⁴⁰. Upon comparing the anisotropic MR in $ZrSiS$ ³³ with our results, we speculate that the anisotropic MR in $ZrSiSe$ may be associated with the quasi-2D nature of the Fermi surface, which is confirmed by band calculations²¹ and ARPES measurements²⁵. Fig. 2(c) displays the amplitude of the angular-dependent SdH oscillations with ϕ varying from 0° to 90° along the bc -plane at 2.3 K. The SdH oscillation amplitude $\Delta\rho$ is obtained from MR measurements after smooth polynomial background subtraction. For better visibility, the oscillation amplitude is plotted in the form of $\Delta\rho/\rho_0$ (where ρ_0 represents the resistivity at zero magnetic field), and the curves are shifted. The oscillation patterns are clearly different for various title angles. Fig. 2(d) shows the corresponding fast Fourier transformation (FFT) spectra of angular-dependent SdH oscillations. We only observe a frequency oscillation of $F = 210$ T when the magnetic

field lies along the c -axis ($\phi = 0^\circ$). Otherwise, the oscillation frequency mode is more than one when the magnetic field is applied along the b -axis ($\phi = 90^\circ$) in the c -plane. These results are consistent with the reported de Haas–van Alphen (dHvA) oscillations of ZrSiSe measured in and out of the c -plane⁷. From FFT amplitude spectra, it is evident that the $F = 210$ T frequency mode always exists and gradually shifts to 460 T as ϕ varies from 0° to 90° . This result indicates that the cross-sectional area of the Fermi surface corresponding to $F = 210$ T does not present the complete 3D case. For the 3D Fermi surface, the corresponding frequency is almost unchanged for different tilt angles of the magnetic field^{7,33,40}. For the 2D Fermi surface, the frequency and its corresponding cross-sectional areas shift following the $1/\cos(\beta)$ law at different tilt angles of magnetic field, where β denotes the tilt angle between the magnetic field and the normal direction of 2D surface^{7,40}. Based on these analyses, we can conclude that 3D and 2D characteristics coexist in the Fermi surface of ZrSiSe. The formula³³ $F = F_1/\cos(t \times \beta)$ can be used to fit the $F = 210$ T frequency mode, where F_1 and t denote fitting parameters. Parameter t is determined by the dimensionality of the Fermi surface, and $t = 0$ and 1 for the 3D and 2D cases, respectively. The tilt angle β is equal to ϕ , namely, the angle between magnetic field and the c -axis of the ZrSiSe crystal. The inset of Fig. 2(c) shows the fitting result, from which the fitting parameters of $F_1 = 210$ T and $t = 0.70$ are obtained. The value of the dimensionality parameter ($t = 0.70$) locates between 0 and 1, which confirms the coexistence of 2D and 3D characteristics for the $F = 210$ T frequency mode. In addition, a low oscillation frequency near $F = 30$ T is also observed with almost no shift with ϕ varying from 30° to 90° , which indicates the 3D property of the Fermi surface.

We also carried out angular-dependent MR measurements of sample 2 in the ac -plane at 2.7 K. The corresponding measurement curve is shown in the inset of Fig. 3(a). The magnetic field is parallel to the current direction when $\phi = 90^\circ$. For clarity, only certain MR curves corresponding to different angles are displayed in Fig. 3(a). Due to the effect of the non-uniform Lorentz force, the MR is very small, and SdH

oscillations are unobservable as the magnetic field lies close to the a -axis. The angular-dependent MR for different magnetic field values is also measured in the ac -plane. As shown in Fig. 3(b), the polar plot exhibits strong anisotropy, similar to the case of the bc -plane [Fig. 2(b)]. The Lorentz force has little effect on the electron movement when the magnetic field lies along the a -axis, thereby resulting in an almost unchanged MR for different field values. Fig. 3(c) shows the oscillation amplitude $\Delta\rho/\rho_0$ with ϕ varying from 0° to 80° at 2.7 K. As in the case of the oscillations in the bc -plane, the different oscillation patterns are evident at various tilt angles. The corresponding FFT spectra are displayed in Fig. 3(d), and the shift of the $F = 210$ T frequency oscillation can be clearly seen with change in ϕ . The dimensionality formula³³ $F = F_1/\cos(t \times \beta)$ is also used to fit the frequency shift of $F = 210$ T. As shown in the inset of Fig. 3(c), the formula fits the experiment frequency shift very well, and fitting parameters of $F_1 = 206$ T and $t = 0.74$ are obtained. The fitting parameters for the bc -plane ($F_1 = 210$ T, $t = 0.70$) and ac -plane ($F_1 = 206$ T, $t = 0.74$) are very close to each other, thereby indicating the almost isotropic nature of the Fermi surface when the magnetic field rotates in the bc -plane and ac -plane. The value of the dimensionality parameter is closer to 1, thereby indicating the presence of the quasi-2D Fermi pocket corresponding to the 210 T SdH oscillation. Otherwise, the low oscillation frequency near $F = 30$ T is also observed when ϕ is varied from 20° to 75° in the ac -plane SdH measurements. This result further reveals the 3D characteristics of the Fermi surface for the $F = 30$ T oscillation. Other than the high and low oscillation frequency modes, there also exist many other frequency modes at large scale angles when the magnetic field changes in the bc -plane and ac -plane. These frequency modes may be related to other Fermi pockets near the Fermi level.

We performed first-principles density functional theory (DFT) calculations to further investigate the properties of the electronic band structures and the Fermi surface in ZrSiSe. Fig. 4(a) shows the calculated band structure of ZrSiSe along various high-symmetry directions in the BZ. The SOC is not considered in our DFT calculations since it has negligible effect on the band structure²⁵. Several Dirac cones

can be observed near the Fermi level, and Dirac-cone-like features are also visible below the Fermi level, which result is very similar to the calculated band structure of ZrSiS^{22,28,31}. These band structure features indicate that electron and hole pockets coexist at the Fermi surface. The corresponding Fermi surface is displayed in Fig. 4(b). As shown in Fig. 4(c), the diamond-shaped Fermi surface formed by the linearly dispersing Dirac cone bands near the Fermi level is clear emerged when observed along the k_z direction. The diamond-shaped Fermi surface is composed of four lens-shaped pockets. In addition, four small quasi-2D tubular-shaped Fermi pockets appear at the corners of the diamond-shaped Fermi surface (X locations in BZ). A similar quasi-2D electrical structure has also been reported in the tubular-shaped Fermi surface of ZrSiS^{8,33,40} and the cylindrical Fermi surface of CeCo₂Ga₈⁴¹. The diamond-shaped Fermi surface around Γ and small pockets near X point have been observed via ARPES measurements in ZrSiS and ZrSiSe^{25,28}. The cross-sectional area of the observed small Fermi pocket near X point is $\sim 3 \times 10^{-2} \text{ \AA}^{-2}$ in ZrSiSe²⁵, consistent with our calculated area order (10^{-2} \AA^{-2}). With the use of the Onsager relation^{34,42,43}, we can obtain the cross-sectional area of the Fermi surface associated with the $F = 210 \text{ T}$ frequency oscillation as $S_F = 2 \times 10^{-2} \text{ \AA}^{-2}$, which value is very close to the area obtained with ARPES measurements at the X point in the BZ²⁵. The cross-sectional area of lens-shaped pockets is evidently larger than that of the tubular-shaped Fermi pockets. This indicates that the $F = 210 \text{ T}$ frequency oscillation corresponds to the small quasi-2D tubular-shaped pocket at X. Recent high-field SdH-oscillation studies have revealed that the high frequency of 240 T in ZrSiS arises from the petal-like Fermi surface pocket near the X point³¹. In addition, Ali et al. have reported on a high frequency of 243 T in ZrSiS, originating from the tubular-shaped Fermi pocket near the X point³³. Due to the usual band features of ZrSiSe, the quasi-2D tubular-shaped Fermi pocket near the X point and other multiple band pockets at the Fermi level simultaneously contribute to the electrical transport. This may be the reason as to why the MR exhibits strong anisotropy.

Conclusion

In conclusion, we systemically performed magnetoresistance measurements and angular-dependent SdH-oscillation analysis in ZrSiSe bulk crystals. The observed nonlinear Hall signal implies the presence of multiple carrier types contributing to the electrical transport. The angular-dependent magnetoresistances in the bc -plane and ac -plane exhibit strong anisotropy, thereby indicating the quasi-2D electronic structure of ZrSiSe. The angular-dependent SdH oscillations indicate the presence multiple of Fermi pockets at the Fermi level. The electronic fermiology of the low oscillation frequency of $F = 30$ T and high oscillation frequency of $F = 210$ T are identified to correspond to the 3D and quasi-2D Fermi pockets, respectively. Our first-principles band calculations further support the presence of multiple band pockets at the Fermi level and confirm the presence of a quasi-2D tubular-shaped Fermi pocket around the X point. The observed strong anisotropic magnetoresistance may be associated with the unusual band structure of ZrSiSe.

Methods

Crystal growth and characterization. Single crystals of ZrSiSe were grown using the chemical vapor transport method with iodine (I_2) as the transport agent. Stoichiometric mixtures of Zr, Si, and Se powder were loaded into a quartz tube with iodine (5 mg/cm^3). The length of the quartz tube used for vapor transport was about 18 cm. The quartz tube was evacuated, sealed, and placed in a horizontal tube furnace such that a temperature gradient was created from $950 \text{ }^\circ\text{C}$ to $850 \text{ }^\circ\text{C}$. The end of the quartz tube that contained the reaction powder was located in the high-temperature zone that was heated to $950 \text{ }^\circ\text{C}$, and the empty end of the quartz tube was maintained at $850 \text{ }^\circ\text{C}$. The quartz tube was kept in the tube furnace for two weeks and then cooled down to room temperature. Finally, plate-like crystals with a metallic luster were obtained at the cold end. The structure of ZrSiSe single crystals was examined by means of a Bruker-D8 ADVANCE X-ray diffractometer (XRD) using $\text{Cu-K}\alpha$ radiation ($\lambda = 1.5406 \text{ \AA}$). The XRD data were collected over the 2θ range of 10° – 60° .

Magnetoresistance measurements. Four-probe measurements of the magnetoresistivity and Hall resistivity were carried out with the use of the Quantum Design Physical Property Measurement System (PPMS-14) system. The electrical properties were measured using the delta method by connecting the Keithley Instruments 6221 and 2182A together.

Electronic structure calculations. The band structures of bulk ZrSiSe were calculated in the framework of density functional theory (DFT) using the WIEN2K code with a full-potential linearized augmented plane-wave. The Perdew–Burke–Ernzerhof (PBE) parameterization of the generalized gradient approximation (GGA) as the exchange–correlation functional was implemented. The irreducible Brillouin zone was sampled by a 15*15*7 mesh of k-points.

References

- 1 Hongming, W., Xi, D. & Zhong, F. Topological semimetals predicted from first-principles calculations. *Journal of Physics: Condensed Matter* **28**, 303001 (2016).
- 2 Du, Y. *et al.* CaTe: a new topological node-line and Dirac semimetal. *npj Quantum Materials* **2**, 3, doi:10.1038/s41535-016-0005-4 (2017).
- 3 Burkov, A. A., Hook, M. D. & Balents, L. Topological nodal semimetals. *Phys. Rev. B* **84**, 235126 (2011).
- 4 Phillips, M. & Aji, V. Tunable line node semimetals. *Phys. Rev. B* **90**, 115111 (2014).
- 5 Weng, H. *et al.* Topological node-line semimetal in three-dimensional graphene networks. *Phys. Rev. B* **92**, 045108 (2015).
- 6 Yu, R., Weng, H., Fang, Z., Dai, X. & Hu, X. Topological Node-Line Semimetal and Dirac Semimetal State in Antiperovskite Cu₃PdN. *Phys. Rev. Lett.* **115**, 036807 (2015).
- 7 Hu, J. *et al.* Evidence of Topological Nodal-Line Fermions in ZrSiSe and ZrSiTe. *Phys. Rev. Lett.* **117**, 016602 (2016).

- 8 Hu, J. *et al.* Nearly massless Dirac fermions and strong Zeeman splitting in the nodal-line semimetal ZrSiS probed by de Haas-van Alphen quantum oscillations. *Phys. Rev. B* **96**, 045127 (2017).
- 9 Li, C.-Z. *et al.* Two-Carrier Transport Induced Hall Anomaly and Large Tunable Magnetoresistance in Dirac Semimetal Cd₃As₂ Nanoplates. *ACS Nano* **10**, 6020-6028, doi:10.1021/acsnano.6b01568 (2016).
- 10 Wang, L.-X., Li, C.-Z., Yu, D.-P. & Liao, Z.-M. Aharonov-Bohm oscillations in Dirac semimetal Cd₃As₂ nanowires. *Nat. Commun.* **7**, 10769, doi:10.1038/ncomms10769 (2016).
- 11 Hasan, M. Z. & Kane, C. L. Colloquium: Topological insulators. *Rev. Mod. Phys.* **82**, 3045-3067 (2010).
- 12 Ando, Y. Topological Insulator Materials. *Journal of the Physical Society of Japan* **82**, 102001, doi:10.7566/JPSJ.82.102001 (2013).
- 13 Castro Neto, A. H., Guinea, F., Peres, N. M. R., Novoselov, K. S. & Geim, A. K. The electronic properties of graphene. *Rev. Mod. Phys.* **81**, 109-162 (2009).
- 14 Hasan, M. Z., Su-Yang, X. & Guang, B. Topological insulators, topological superconductors and Weyl fermion semimetals: discoveries, perspectives and outlooks. *Physica Scripta* **2015**, 014001 (2015).
- 15 Chen, T. *et al.* High-Mobility Sm-Doped Bi₂Se₃ Ferromagnetic Topological Insulators and Robust Exchange Coupling. *Advanced Materials* **27**, 4823-4829, doi:10.1002/adma.201501254 (2015).
- 16 Chen, T. *et al.* Topological transport and atomic tunnelling–clustering dynamics for aged Cu-doped Bi₂Te₃ crystals. *Nat. Commun.* **5**, 5022, doi:10.1038/ncomms6022 (2014).
- 17 Shuai Zhang *et al.* Stepwise quantized surface states and delayed Landau level hybridization in Co cluster-decorated BiSbTeSe₂ topological insulator devices. *arXiv:1702.03344v1* (2017).
- 18 Wang, L.-X. *et al.* Zeeman effect on surface electron transport in topological insulator Bi₂Se₃ nanoribbons. *Nanoscale* **7**, 16687-16694,

- doi:10.1039/C5NR05250E (2015).
- 19 Bian, G. *et al.* Topological nodal-line fermions in spin-orbit metal PbTaSe₂. *Nat. Commun.* **7**, 10556, doi:10.1038/ncomms10556 (2016).
- 20 Wu, Y. *et al.* Dirac node arcs in PtSn₄. *Nat. Phys.* **12**, 667-671, doi:10.1038/nphys3712 (2016).
- 21 Xu, Q. *et al.* Two-dimensional oxide topological insulator with iron-pnictide superconductor LiFeAs structure. *Phys. Rev. B* **92**, 205310 (2015).
- 22 Schoop, L. M. *et al.* Dirac cone protected by non-symmorphic symmetry and three-dimensional Dirac line node in ZrSiS. *Nat. Commun.* **7**, 11696, doi:10.1038/ncomms11696 (2016).
- 23 Andreas, T. *et al.* Non-symmorphic band degeneracy at the Fermi level in ZrSiTe. *New Journal of Physics* **18**, 125014 (2016).
- 24 Chen, C. *et al.* Dirac line nodes and effect of spin-orbit coupling in the nonsymmorphic critical semimetals MSiS (M=Hf,Zr). *Phys. Rev. B* **95**, 125126 (2017).
- 25 Hosen, M. M. *et al.* Tunability of the topological nodal-line semimetal phase in ZrSiX-type materials (X=S, Se, Te). *Phys. Rev. B* **95**, 161101 (2017).
- 26 Lou, R. *et al.* Emergence of topological bands on the surface of ZrSnTe crystal. *Phys. Rev. B* **93**, 241104 (2016).
- 27 Takane, D. *et al.* Dirac-node arc in the topological line-node semimetal HfSiS. *Phys. Rev. B* **94**, 121108 (2016).
- 28 Neupane, M. *et al.* Observation of topological nodal fermion semimetal phase in ZrSiS. *Phys. Rev. B* **93**, 201104 (2016).
- 29 Sankar, R. *et al.* Crystal growth of Dirac semimetal ZrSiS with high magnetoresistance and mobility. *7*, 40603, doi:10.1038/srep40603 (2017).
- 30 Lv, Y.-Y. *et al.* Extremely large and significantly anisotropic magnetoresistance in ZrSiS single crystals. *Appl. Phys. Lett.* **108**, 244101, doi:10.1063/1.4953772 (2016).
- 31 S. Pezzini *et al.* Unconventional mass enhancement around the Dirac nodal

- loop in ZrSiS. *arXiv:1701.09119* (2017).
- 32 Wang, X. *et al.* Evidence of Both Surface and Bulk Dirac Bands and Anisotropic Nonsaturating Magnetoresistance in ZrSiS. *Adv. Electron. Mater.* **2**, 1600228-n/a, doi:10.1002/aelm.201600228 (2016).
- 33 Ali, M. N. *et al.* Butterfly magnetoresistance, quasi-2D Dirac Fermi surface and topological phase transition in ZrSiS. *Science Advances* **2**, doi:10.1126/sciadv.1601742 (2016).
- 34 Kumar, N. *et al.* Unusual magnetotransport from Si-square nets in topological semimetal HfSiS. *Phys. Rev. B* **95**, 121109 (2017).
- 35 Zhao, Y. *et al.* Anisotropic magnetotransport and exotic longitudinal linear magnetoresistance in WTe₂ crystals. *Phys. Rev. B* **92**, 041104 (2015).
- 36 Thoutam, L. R. *et al.* Temperature-Dependent Three-Dimensional Anisotropy of the Magnetoresistance in WTe₂. *Phys. Rev. Lett.* **115**, 046602 (2015).
- 37 Kumar, N. *et al.* Observation of pseudo-two-dimensional electron transport in the rock salt-type topological semimetal LaBi. *Phys. Rev. B* **93**, 241106 (2016).
- 38 Zhu, Z., Collaudin, A., Fauque, B., Kang, W. & Behnia, K. Field-induced polarization of Dirac valleys in bismuth. *Nat. Phys.* **8**, 89-94, doi:10.1038/nphys2111 (2012).
- 39 Collaudin, A., Fauqué, B., Fuseya, Y., Kang, W. & Behnia, K. Angle Dependence of the Orbital Magnetoresistance in Bismuth. *Phys. Rev. X* **5**, 021022 (2015).
- 40 Singha, R., Pariari, A. K., Satpati, B. & Mandal, P. Large nonsaturating magnetoresistance and signature of nondegenerate Dirac nodes in ZrSiS. *Proceedings of the National Academy of Sciences* **114**, 2468-2473, doi:10.1073/pnas.1618004114 (2017).
- 41 Wang, L. *et al.* Heavy fermion behavior in the quasi-one-dimensional Kondo lattice CeCo₂Ga₈. *npj Quantum Materials* **2**, 36, doi:10.1038/s41535-017-0040-9 (2017).

- 42 Pan, H. *et al.* Quantum oscillation and nontrivial transport in the Dirac semimetal Cd₃As₂ nanodevice. *Appl.Phys. Lett.* **108**, 183103, doi:10.1063/1.4948654 (2016).
- 43 He, L. P. *et al.* Quantum transport evidence for the three-dimensional Dirac semimetal phase in Cd₃As₂. *Phys. Rev. Lett.* **113**, 246402, doi:10.1103/PhysRevLett.113.246402 (2014).

Acknowledgements

We gratefully acknowledge the financial support of the National Key Projects for Basic Research of China (Grant No: 2013CB922103), the National Program on Key Basic Research Project of China (Grant No: 2017YFA0303200), the National Natural Science Foundation of China (Grant Nos: 91421109, 91622115, 11522432, 61176088 and 11274003), the Natural Science Foundation of Jiangsu Province (Grant BK20160659, BK20130054), and the Fundamental Research Funds for the Central Universities (Grant Nos: 020414380056, 020414380057).

Author Contributions

H.P. and F.S. conceived the work and wrote the paper. The single crystals were grown and characterized by H.P. and J.W.. H.P., D.F., S.Z. and B.W. carried out the low temperature transport measurements. J.Y. and X.W. performed the theoretical band calculations.

Additional information

Competing financial interests: The authors declare no competing financial interests.

Figures

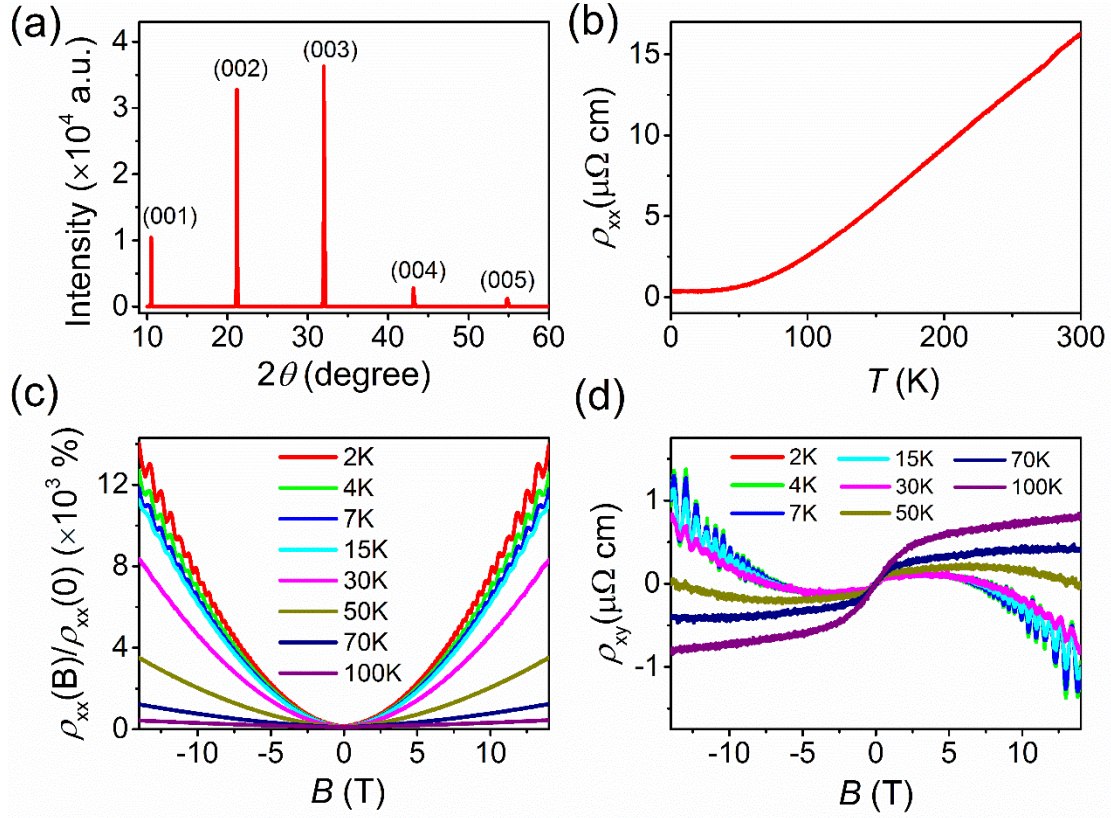


Figure 1. X-ray diffraction and electrical transport in ZrSiSe bulk crystals (sample 1).

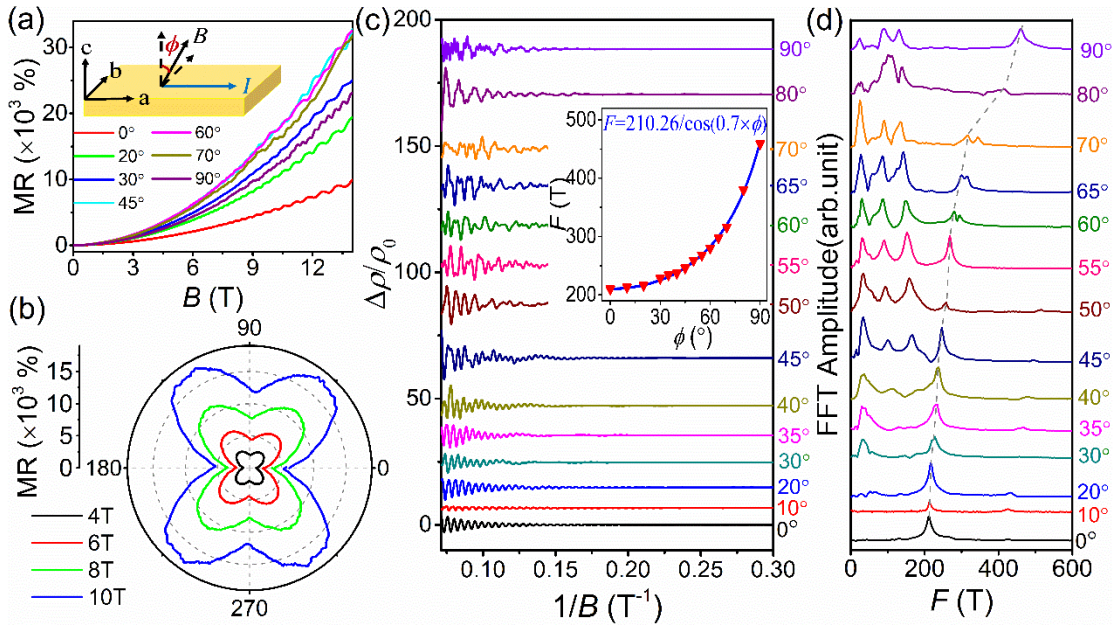


Figure 2. Angular-dependent Shubnikov-de Haas (SdH) oscillations of transverse magnetoresistance (MR) at 2.3 K with magnetic field B rotated in the bc -plane for sample 2.

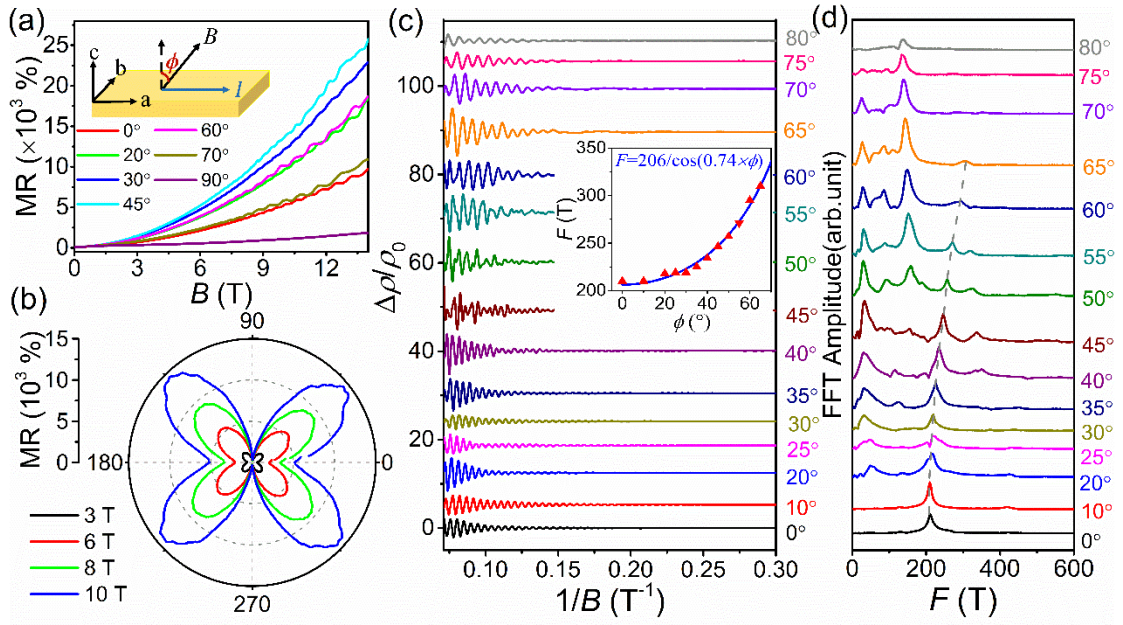


Figure 3. Angular-dependent Shubnikov-de Haas (SdH) oscillations of magnetoresistance (MR) at 2.7 K with magnetic field B rotated in the ac -plane for sample 2.

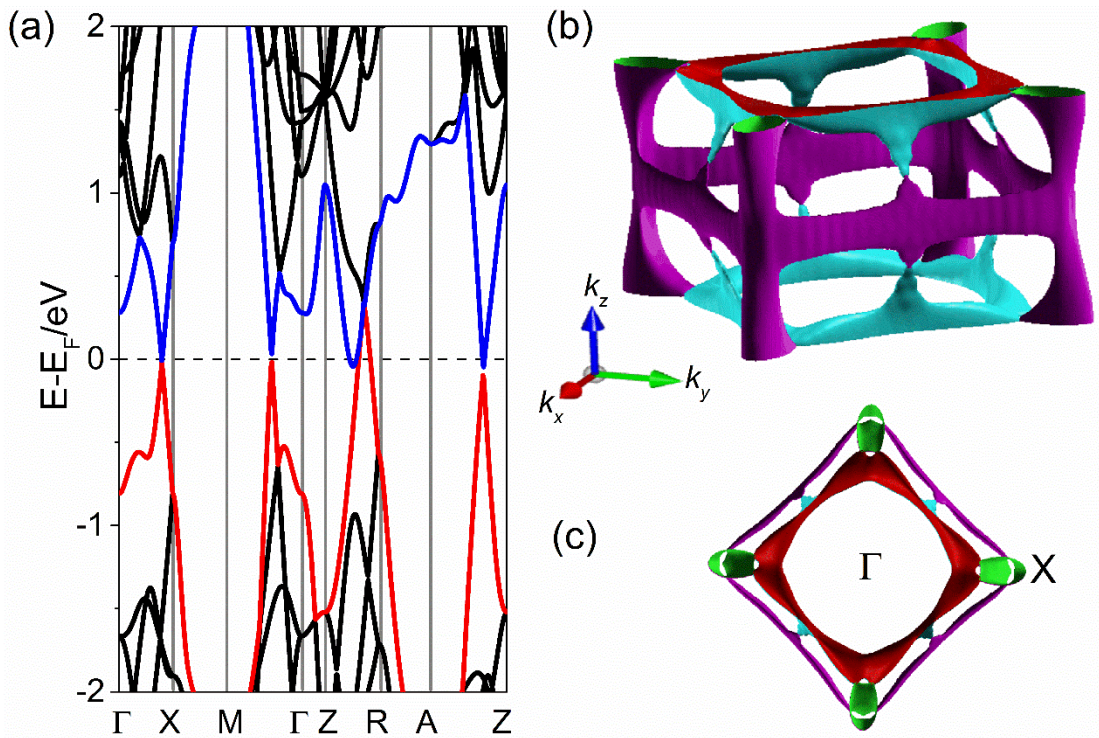


Figure 4. Calculated band structure and Fermi surface of bulk ZrSiSe.

Figure legends

Figure 1. X-ray diffraction and electrical transport in ZrSiSe bulk crystals (sample 1). (a) X-ray diffraction (XRD) patterns of a typical single crystal of ZrSiSe. The XRD peak position indicates that the sample surface lies along the (001) plane. (b) Temperature-dependent longitudinal resistivity at zero magnetic field. (c) Ratio of magnetoresistivity $\rho_{xx}(B)/\rho_{xx}(0)$ at different temperatures. (d) Corresponding Hall resistivity measured at different temperatures.

Figure 2. Angular-dependent Shubnikov–de Haas (SdH) oscillations of transverse magnetoresistance (MR) at 2.3 K with magnetic field B rotated in the bc -plane for sample 2. (a) MR measured at different angles with ϕ varying from 0° to 90° . For clarity, only certain MR curves for different angles are displayed. The inset shows the schematic for the field rotation in the bc -plane. (b) Polar plot of angular-dependent MR for different magnetic fields along the bc -plane. (c) SdH oscillation amplitude (after polynomial background subtraction) measured with ϕ varying from 0° to 90° . The inset shows the angular-dependent frequency of SdH oscillations. (d) Corresponding fast Fourier transform (FFT) amplitude spectra of angular-dependent SdH oscillations in the bc -plane.

Figure 3. Angular-dependent Shubnikov–de Haas (SdH) oscillations of magnetoresistance (MR) at 2.7 K with magnetic field B rotated in the ac -plane for sample 2. (a) MR measured at different angles with ϕ varying from 0° to 80° . For clarity, only certain magnetoresistance curves for different angles are displayed. The inset shows the schematic for the field rotation in the ac -plane. (b) Polar plot of angular-dependent MR for different magnetic fields along the ac -plane. (c) SdH oscillation amplitude (after polynomial background subtraction) measured with ϕ varying from 0° to 80° . The inset shows the angular-dependent frequency of SdH

oscillations. **(d)** Corresponding fast Fourier transform (FFT) amplitude spectra of angular-dependent SdH oscillations in the ac -plane.

Figure 4. Calculated band structure and Fermi surface of bulk ZrSiSe. **(a)** Calculated band structure along various high-symmetry directions without considering spin-orbit coupling. **(b)** Corresponding 3D Fermi surfaces of ZrSiSe in reciprocal space. **(c)** Detailed Fermi surface as observed along the k_z direction.